



Effect of Nb and Fe co-doping on microstructure, dielectric response, ferroelectricity and energy storage density of PLZT

Shibnath Samanta¹ · V. Sankaranarayanan¹ · K. Sethupathi¹

Received: 22 July 2018 / Accepted: 4 October 2018 / Published online: 6 October 2018
© Springer Science+Business Media, LLC, part of Springer Nature 2018

Abstract

The studies on the effect of simultaneous doping of donor (Nb) and acceptor (Fe) (0–8 at.% of each dopant) in PLZT ($\text{Pb}_{0.97}\text{La}_{0.02}\text{Zr}_{0.52}\text{Ti}_{0.48}\text{O}_3$), on the dielectric response, ac conductivity and ferroelectricity are reported in this article. It is observed that the value of dielectric constant decreases, dielectric loss increases (moderately) and coercive field increases upon doping of Nb and Fe together. These indicate a hardening like effect as a result of the donor–acceptor co-doping. The ferroelectric to paraelectric phase transition occurs at lower temperatures for higher doping concentrations. For undoped PLZT the Curie temperature is around 353 °C which shifts to 305 °C for 8% Nb–Fe co-doped PLZT. Microstructure studies on the surface, as well as the interior of the samples are carried out which reveal a clear difference. The grain size is observed to decrease with doping concentration. The “true switchable polarization” is deduced by positive up negative down (PUND) tests and found to decrease with doping. Fatigue behavior is found to be positively enhanced upon co-doping of 2% Nb and Fe. Leakage current tests are carried out and it is found that the samples become more ‘leaky’ upon co-doping of Nb and Fe. The energy storage density is also investigated for these Nb–Fe co-doped PLZT ceramics. The highest recoverable energy storage density is observed for 2% Nb–Fe co-doped PLZT sample and it is around 134 mJ/cm³ with an efficiency of 0.28.

1 Introduction

The study reported by Carl and Hardtl in Ref. [1], on internal bias field induced by the incorporation of various dopants in PZT ($\text{Pb}(\text{Zr},\text{Ti})\text{O}_3$), resulting as constriction of hysteresis loop or increase in dielectric and mechanical losses due to pinning of domain walls or rising anisotropy is considered as the discovery of the soft and hard PZT [2]. The acceptor doping (i.e. a monovalent cation replacing Pb or a trivalent replacing Zr/Ti) leads to the stabilization of domain wall that makes poling and depoling processes difficult, thereby, increasing the coercive field. On the other hand, donor doping (i.e. a trivalent cation replacing Pb or a pentavalent replacing Zr/Ti) exhibits low coercive field, high piezoelectric coefficient, high dielectric loss, low conductivity and

does not show hardening effect. This is how the acceptor and donor doped PZTs are termed as hard and soft PZTs respectively [3].

Studies on soft PZTs in which Pb^{2+} replaced by La^{3+} and Zr/Ti^{4+} replaced by Nb^{5+} and hard PZTs where Zr/Ti^{4+} replaced by Fe^{3+} are reported in literature several times. Nb-doping was found to influence dielectric and ferroelectric properties by altering microstructure and pyrochlore phase formation [4]. In fact, Nb-doping was proved to be helpful in enhancing the dielectric and piezoelectric properties [5]. In addition, improvement in fatigue behavior and a decrease in the coercive field due to Nb-doping were also reported [6]. In the case of La^{3+} incorporated PZT, the doping modifies domain walls and also improves the remnant polarization, coercive field, shape of the hysteresis loops, dielectric and piezoelectric properties [7]. Lee et al. reported that complex doping of La and Nb together in PZT (53/47) improves the piezoelectric effect while the addition of Fe to these compositions leads to decrease in dielectric constant and planar coupling factor [8]. However, this report demonstrated the doping of La, Nb and Fe up to 1.8, 2.2 and 2% respectively only in three complex combinations. Hence, it remains difficult to understand the effect of the complex doping.

✉ Shibnath Samanta
shibnaths2@gmail.com

✉ K. Sethupathi
ksethu@iitm.ac.in

V. Sankaranarayanan
vsn@iitm.ac.in

¹ Department of Physics, Indian Institute of Technology Madras (IITM), Chennai 600036, India

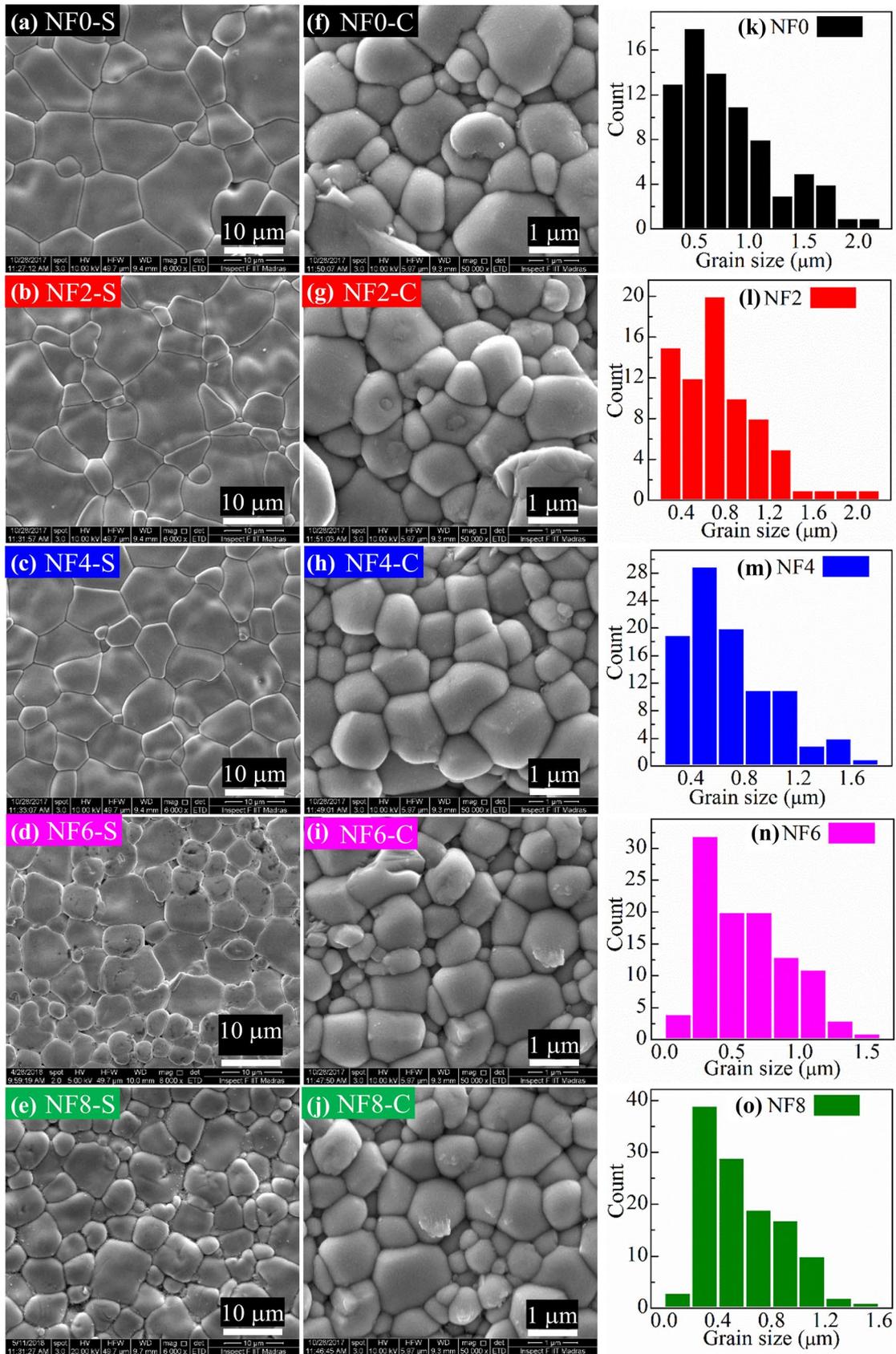


Fig. 1 Microstructure of Nb and Fe co-doped PLZT. **a–e** show SEM images of the surface of the samples at $\times 6000$ magnification. **f–j** show SEM images of the cross-sections of the samples at $\times 50,000$ magnification. The alphabets “S” and “C” represent surface and cross-section respectively. **k–o** are the histograms of grain size as observed in cross-sectional micrographs

Considering the above facts, it is important to study the effect of systematic and simultaneous doping of both donor and acceptor in PZT. The properties of pure PZTs are often affected by defects related to oxygen vacancies and lead vacancies. Oxygen vacancies occur as a result of charge imbalance due to Pb-loss [3]. A suitable amount of La^{3+} incorporation reduces these defects and increases tetragonality. Thus 2% La-doping in bulk PZT [9] and 0.5% La doping in PZT thin film [10] show enhanced ferroelectricity. In our present work, keeping these into account, Nb and Fe co-doped $\text{Pb}_{0.97}\text{La}_{0.02}\text{Zr}_{0.52}\text{Ti}_{0.48}\text{O}_3$ (PLZT) are studied. Here, it is worth to mention that in 2009, Kleebe et al. reported successful preparation and characterization of 3% Fe-doped $\text{PbZr}_{0.6}\text{Ti}_{0.4}\text{O}_3$ which is greater than the solubility limit (approximately 1% Fe^{3+} in $\text{PbZr}_{0.6}\text{Ti}_{0.4}\text{O}_3$) [11]. However, up to 8% of Fe-doping is possible (as co-dopant with Nb of the same amount as Fe) in PLZT [12]. The Nb^{5+} and Fe^{3+} have crystal ionic radii ~ 78 and 69 pm, respectively (effective ionic radii ~ 64 and 55 pm, respectively), while the corresponding values for Zr^{4+} and Ti^{4+} are 86 and 74.5 pm, respectively (effective ionic radii ~ 72 and 60.5 pm, respectively). The ionic radius of Fe^{3+} is smaller than that of the average radius of Zr^{4+} and Ti^{4+} but the ionic radius of Nb^{5+} is comparable to the average radius of Zr^{4+} and Ti^{4+} . If only Fe^{3+} is doped, the charge imbalance causes stoichiometric change thereby inducing oxygen deficiency. Sufficient amount of oxygen deficiency promotes structural instability. Hence, the addition of Nb^{5+} helps reducing charge imbalance and thereby stabilizing the structure. This could be the probable cause of how the effective solubility of Fe increases while co-doped with Nb. However, as the ionic radius of Fe^{3+} is smaller than that of Zr^{4+} and Ti^{4+} , there must be a certain limit for doping. In our study, it appears to be around 8%, but detailed investigations regarding this are required to confirm the above facts. The preparation and characterization (structure, lattice vibration and band gap) of these Nb and Fe co-doped PLZT are reported in our previous paper [12]. In the present article, the studies on the dielectric response, ac conductivity, ferroelectricity and energy storage density of those Nb and Fe co-doped PLZT are presented.

2 Experimental procedure

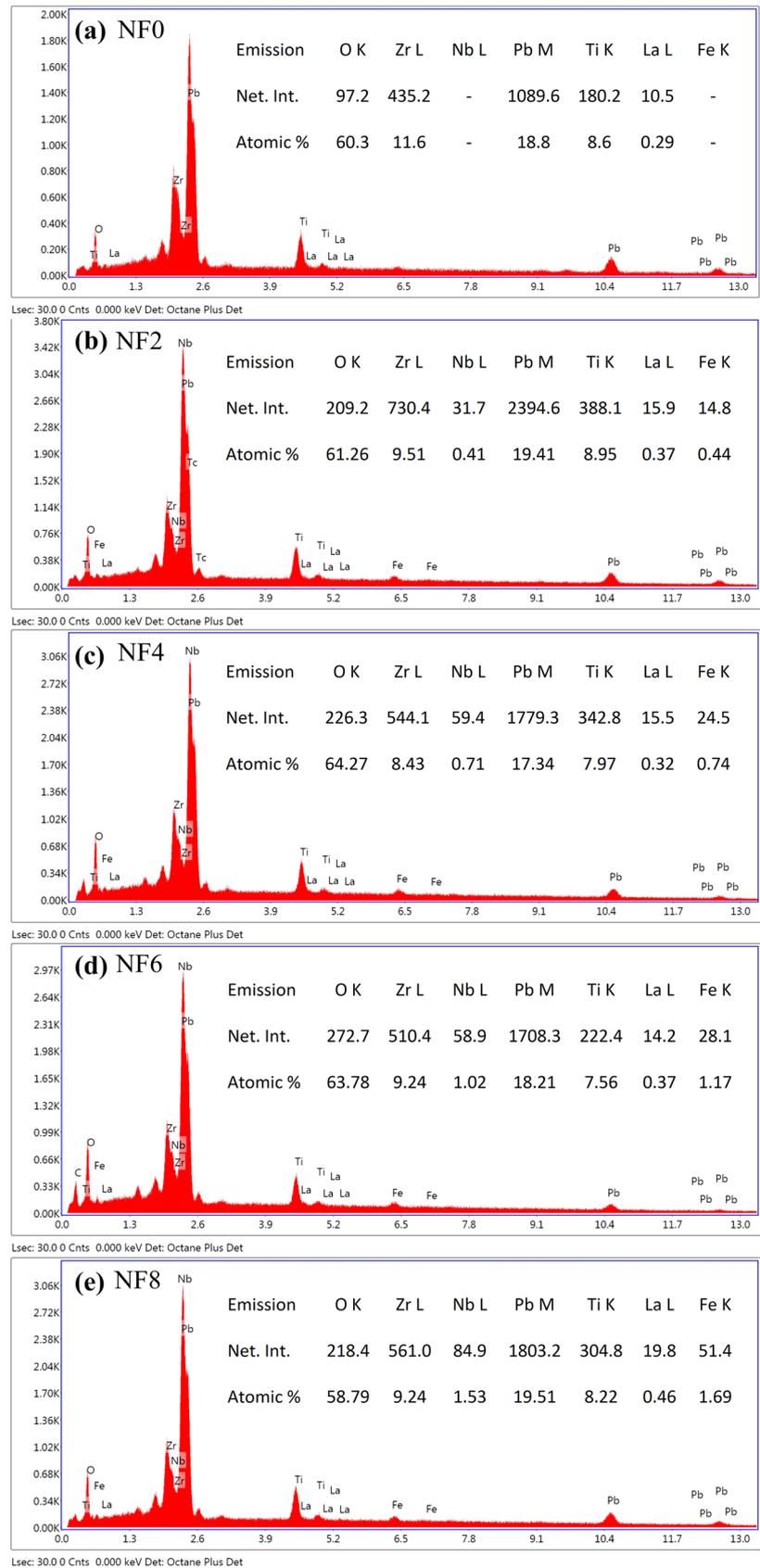
$\text{Pb}_{0.97}\text{La}_{0.02}(\text{Zr}_{0.52}\text{Ti}_{0.48})_{1-2x}(\text{Nb}_{0.5}\text{Fe}_{0.5})_{2x}\text{O}_3$ for $x = 0.00, 0.02, 0.04, 0.06$ and 0.08 (will be denoted hereafter as NF0, NF2, NF4, NF6 and NF8, respectively) are prepared by sol-gel synthesis. Lead(II) acetate trihydrate (99.999%), Lanthanum(III) acetate hydrate (99.9%), Niobium(V) ethoxide (99.95%), Zirconium(IV) propoxide solution (70 wt% in 1-propanol), Titanium(IV) isopropoxide (97%) and Ferric(III) nitrate nonahydrate (99.95%) are used as precursors. Details of the alkoxide based sol-gel synthesis and the flowchart can be found elsewhere [12]. The powder obtained by the above synthesis is pressed at 100 kg/cm^2 pressure to get them into pellet form. These green bodies are solidified by a “double atmospheric layer protected sintering (DALPS)” method [9]. The sintered pellets are used for scanning electron microscopy (FEI Inspect F). Silver paste (SPI high purity silver paint) was applied on the flat surfaces of the pellets to get proper electrode contacts for electrical measurements. The dielectric and ferroelectric studies are carried out using Broadband impedance analyzer (Novo-Control Technology) and Precision Premier II (Radiant Technology).

3 Results and discussion

3.1 Microstructure

In general, the morphology of a sintered pellet surface is different from that of the interior of the sample though most of the reports show the morphology of either the as-sintered surface or polished one. We have investigated microstructure on the surface as well as the interior of the sample. Figure 1a–e show the SEM micrographs of the surface of the samples NF0, NF2, NF4, NF6 and NF8, respectively. The surface microstructures consist of grains of random shapes. Defects such as pores, cracks or discontinuities are rarely observed. The size of the grains on the surface is observed to decrease with increasing doping concentration. On the surface of NF0, the grain size varies between 1 and $19 \mu\text{m}$ whereas the grains are 0.5 – $10.5 \mu\text{m}$ on the surface of NF8. The average grain sizes are $7.92, 7.15, 6.71, 5.02$ and $4.52 \mu\text{m}$ for NF0, NF2, NF4, NF6 and NF8, respectively. Elemental presence is observed from the ‘eZAF quantization results’ on the Energy dispersive X-ray spectroscopy (EDS) recorded on the cross-sectional surfaces of the samples. The EDS spectra are shown in Fig. 2. The presence of Nb L and Fe K in these spectra confirms the incorporation of Nb and Fe in PLZT. The systematic increase in the atomic % of Nb and Fe is also notable from NF0 to NF8 samples.

Fig. 2 Energy dispersive X-ray spectroscopy (EDS) spectra with elemental presence, recorded on the cross-sectional surfaces of NF0, NF2, NF4, NF6 and NF8



To observe the microstructure deep inside the samples, the samples are broken and SEM is carried out on the points approximately at the midway of the thickness. The micrographs obtained are shown in Fig. 1f–j. The grain size distribution in the interior of the samples is analyzed with the help of ImageJ software and the histograms are shown in Fig. 1k–o. One can clearly see that there is a difference between the surface morphology and the interior microstructure. The grains inside the sample are much smaller than those on the surface. Grains of size 0.3–2.1 μm with an average size of 0.82 μm are observed inside NF0. For NF2 sample, the grain size range is the same but the number of smaller grains is marginally higher and hence the average size reduced to 0.76 μm . With increasing Nb–Fe co-doping concentration, the grain size decreases gradually. Grains are of size 0.1–1.7 μm and 0.1–1.5 μm inside NF4 and NF6 in which average grain size is observed to be 0.61 and 0.69 μm respectively. Though the change in grain size with doping concentration is small, it has consistency and shows the effect of the doping.

3.2 Dielectric properties

Dielectric responses of NF0, NF2, NF4, NF6 and NF8 samples are recorded from 30 to 370 $^{\circ}\text{C}$ for frequencies between 100 Hz and 1 MHz. The room temperature tests are made for 10 Hz to 10 MHz. The dielectric behavior is shown in Fig. 3a. The value of dielectric constant (ϵ_r') decreases with frequency. It drops sharply at lower frequencies but the rate of decrease is less at frequencies higher than 10^3 Hz. On the other hand, the value of loss tangent ($\tan \delta$) falls rapidly up to 10^5 Hz and suddenly increases afterwards. The value of ϵ_r' decreases (1368 for NF0 to 858 for NF8 at 1 kHz) when 8% of Nb and Fe is incorporated, whereas $\tan \delta$ shows a clear increase from 0.049 to 0.112 for a frequency of 100 Hz. However, at 1 kHz the values of $\tan \delta$ are 0.016, 0.014, 0.016, 0.019 and 0.021 for NF0, NF2, NF4, NF6 and NF8 respectively i.e. it does not increase systematically (like it does at 100 Hz) owing to a crossover between 10^3 and 10^4 Hz, above which $\tan \delta$ appears to decrease upon increase in doping. The high value of $\tan \delta$ at lower frequencies may be due to the large contribution of loss from the Maxwell–Wagner interfacial polarization [7]. Thus, as interfacial polarization decreases with frequency, the $\tan \delta$ also decreases with frequency up to 10^4 – 10^5 Hz. At higher frequencies, the value of $\tan \delta$ increases as dielectric constant decreases and the frequency dependent conduction increases with frequency. Sometimes this relaxation at higher frequencies are considered as the glass transition relaxation [13, 14]. The decrease in the value of ϵ_r' with doping concentration at room temperature observed from Fig. 3a could be due to the decrease in grain size with doping along with the other

causes like a change in defect dipole formation and lattice structural change due to doping.

Figure 3b exhibits the temperature dependence of ϵ_r' at different frequencies for NF0. The value of ϵ_r' is observed to increase with temperature and above 200 $^{\circ}\text{C}$, a sharp increase followed by a dramatic fall can be noted. The peak at 353 $^{\circ}\text{C}$ corresponds to the ferroelectric to paraelectric transition. The transition temperature i.e. the Curie temperatures (T_C) for NF2 (Fig. 3c), NF4 (Fig. 3d), NF6 (Fig. 3e) and NF8 (Fig. 3f) are 335, 325, 314 and 305 $^{\circ}\text{C}$ respectively. This indicates that the Nb and Fe co-doping advances the ferro-para transition and around 48 $^{\circ}\text{C}$ decrements happen due to 8% of Nb and Fe present in the lattice. It is also notable that the value of ϵ_r' at T_C i.e. $\epsilon_r'_{\text{max}}$ decreases from 25,385 (for NF0 at 1 kHz) to 6054 (for NF8 at 1 kHz). The peaks in $\tan \delta$ versus temperature profiles follow a similar trend as that of the ϵ_r' . The degradation in ϵ_r' values with increase in frequency is more at higher temperatures. The similar trend is observed in all the samples. The frequency dispersion of dielectric constant has four distinct ranges of temperature. At temperatures below 200 $^{\circ}\text{C}$, the variation with temperature is minimal and above 200 $^{\circ}\text{C}$, the frequency dependence becomes prominent and stronger as temperature rises. Around T_C , the dielectric constant has a stronger dependence on frequency, while above T_C the behavior is the same as that observed between the temperature range 200 $^{\circ}\text{C}$ and T_C . This happens due to (i) dipole formation from dopant ions and defects, (ii) behavior of oxygen vacancies as charge carriers, and (iii) thermally activated conduction being both frequency and temperature dependent. The observed frequency dispersion is the outcome of complex effects of these factors [15]. The change in $\tan \delta$ value with frequency is higher at high temperatures but shows dissimilar trends at a different range of temperatures though not exactly similar to that of dielectric constant. In the temperature range – 100 to 70 $^{\circ}\text{C}$, the degree of changes with frequency are very marginal with respect to the changes observed at other temperatures. In the temperature range between 70 and 280 $^{\circ}\text{C}$, for higher frequencies the values of $\tan \delta$ are higher whereas above 280 $^{\circ}\text{C}$, the value is lower for higher frequencies. The amount of change is also higher in this temperature range. The above-described behavior is consistent for all doping concentrations.

For samples with higher doping concentrations (NF4, NF6 and NF8), a raising part in $\tan \delta$ versus temperature could be observed after the transition around 355 $^{\circ}\text{C}$ (NF4) which shifts towards lower temperatures for higher doping i.e. 343 $^{\circ}\text{C}$ for NF6 and 338 $^{\circ}\text{C}$ for NF8. This rise may be due to the fact that the dielectric loss could increase due to the thermally activated conduction because of which the materials lose energy as heat. Thus, this process is promoted by the doping, and as a result, it becomes visible at lower temperatures (lower than 355 $^{\circ}\text{C}$) for a higher amount of

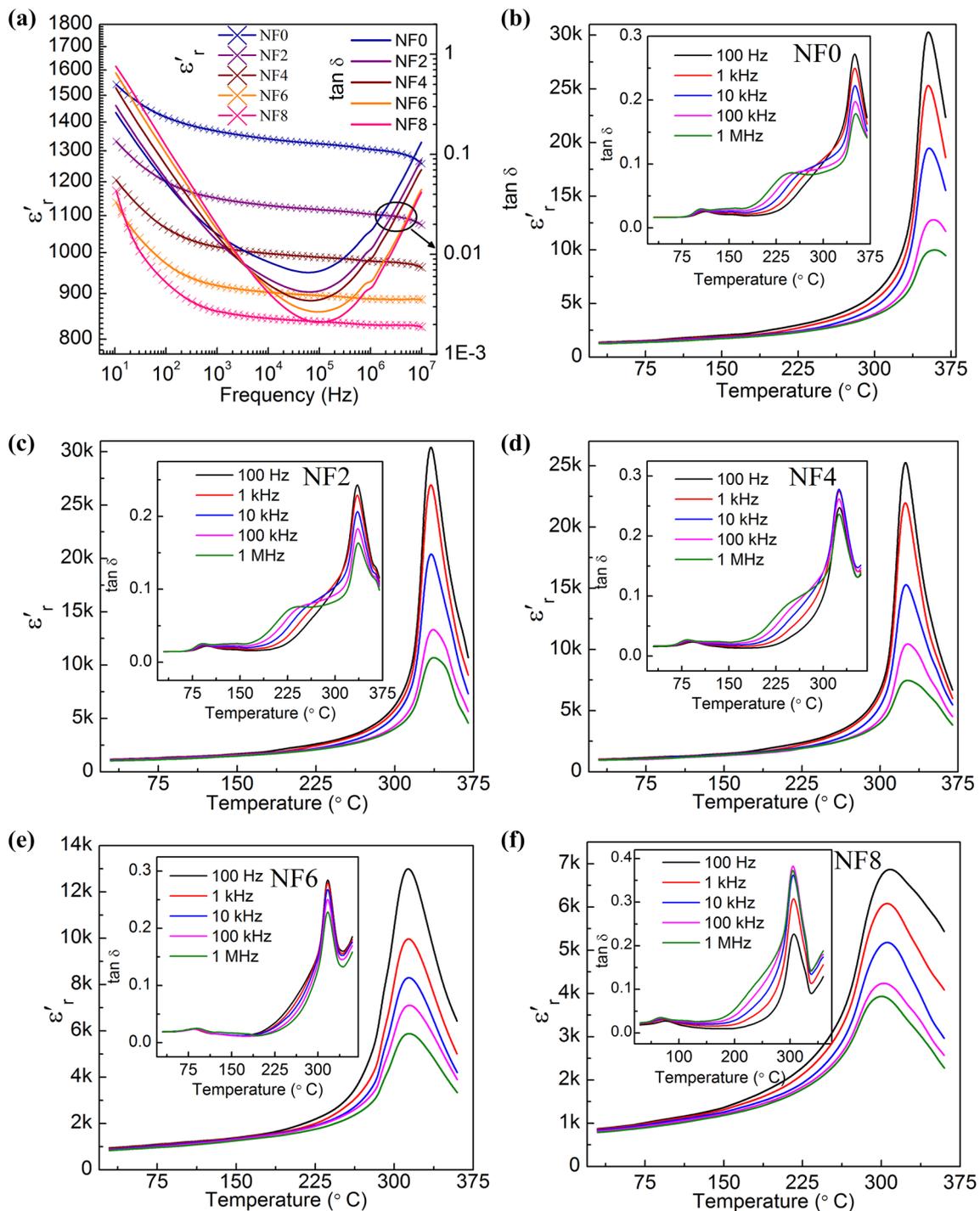


Fig. 3 Dielectric properties of Nb and Fe co-doped PLZT. **a** Frequency dependence of dielectric constant (ϵ_r') and loss tangent ($\tan \delta$). **b–f** Temperature dependence of ϵ_r' of NF0, NF2, NF4, NF6 and NF8. Insets are corresponding temperature dependence of $\tan \delta$

doping. Here, it should be noted that for NF0 and NF2 samples this may happen at further higher temperatures, which are beyond our experimental limit.

3.3 AC conductivity and specific resistance

The frequency dependence of conductivity, suggested by Jonscher's power relation [16, 17] is

$$\sigma_T(\omega) = \sigma(0) + K\omega^n \quad (1)$$

where, σ_T , $\sigma(0)$, K , n and ω are total conductivity, dc conductivity, pre-exponent, exponent and frequency respectively. Generally, the value of $\sigma(0)$ is several orders smaller than the ac conductivity in a ferroelectric material. Such a material can be considered as randomly connected series and parallel RC network formed by the microstructures. The grains act as capacitors (C), while the grain boundaries are resistors (R). In such a case it follows a logarithmic mixing rule. If α is the fraction of capacitors then the complex conductivity σ^* can be written as [18]

$$\sigma^* = (i\omega C)^\alpha (R^{-1})^{(1-\alpha)} \quad (2)$$

$$\sigma^* = \sigma' - i\sigma'' = \frac{1}{Z^*(\omega)} \frac{d}{A} \quad (3)$$

(σ' , σ'' , Z^* , d and A are the real part of conductivity, the imaginary part of conductivity, complex impedance, electrode spacing and electrode area respectively). The temperature dependence of σ' , σ'' and ρ (specific resistance) for NF-samples at different frequencies are shown in Fig. 4. Both the σ' and σ'' values are observed to increase with temperature with a peak around the Curie temperature. There can be several mechanisms involved in the conduction process in a ferroelectric material. One such process is ionic conduction which becomes effective at high temperatures [19], and is termed as “thermally activated conduction”. Additionally, the sharp increase in conductivity around the Curie point could be due to the increase in polarizability at the ferro-para phase transition [20]. The temperature response of specific resistance is shown in Fig. 4k–o. The specific resistance decreases with temperature which (except in the region around ferro-para phase transition) is similar to the behavior of a semiconductor. In this context, it is worth to recall that these samples are wide band gap semiconductor with the values of band gap around 2.6–3.2 eV [12].

The second important observation from Fig. 4 is the frequency dispersion of both σ' and σ'' . The conductivity is observed to increase with frequency. From the microstructural view, as discussed above, an increase in ac conductivity with frequency is expected as the complex conducting paths in materials increase with frequency [18]. At higher frequencies, the ac current flows through the complex sets of the network connecting all the components. The frequency response of conductivity differs at different temperatures. At lower temperatures, conductivity increases faster with frequency. For example, at room temperature, it increases from 10^{-8} to 10^{-6} S/cm two orders in magnitude, for a change of frequency from 100 Hz to 1 MHz for the NF0 sample. As the temperature increases, the frequency dispersion decreases. For the same sample, the change is less than one order at the highest temperature (370 °C which we could obtain). According to the power law relation: at lower frequencies, ac conductivity is strongly sensitive to temperature but at

higher frequencies, it is comparatively less affected by temperature. Hence, the behavior observed is as expected [21].

3.4 Ferroelectricity

NF0 sample shows very high polarization value with high remnant. For an electric field of 35 kV/cm, the observed maximum polarization (P_{\max}) and remnant polarization (P_r) are respectively 43.52 and 38.45 $\mu\text{C}/\text{cm}^2$. The reasons behind the observation of this high polarization values in NF0 (i.e. 2% La-doped PZT(52/48)) are the precise amount of La-doping in the morphotropic phase boundary composition and the use of the highly efficient atmospheric sintering process [9]. La-doping increases the domain wall mobility, compensates charge loss due to Pb-loss and increases the tetragonality, when incorporated with the precise amount. It is found that for thin films 0.5% [10] and for bulk 2% [9] of La-doping shows enhancement in ferroelectricity.

Upon incorporation of 2 at.%, of Nb and Fe, the polarization sharply falls from the above said values (P–E loops are shown in Fig. 5). The observed P_{\max} and P_r for NF2 are 33.38 and 22.01 $\mu\text{C}/\text{cm}^2$ respectively. With increasing doping concentration both these polarizations are found to decrease. The values of P_{\max} are 27.49, 22.25 and 18.89 $\mu\text{C}/\text{cm}^2$ for NF4, NF6 and NF8 respectively. Similarly, the values of P_r observed are 20.47, 15.13 and 15.49 $\mu\text{C}/\text{cm}^2$. The value of P_r for NF8 is almost the same as that of NF6 which is probably a direct consequence of the fact that the tetragonality of NF8 is nearly equal to that of NF6 [12]. In addition, the polarization maximum for NF8 sample occurs around 20 kV/cm and at further higher fields, the value decreases. A similar observation can also be found in the leakage current discussed later. This increase in the leakage current for higher doped samples at higher fields causes the decrease in the polarization as observed in NF8 at fields higher than 20 kV/cm. A similar observation can also be noted from earlier reports [22, 23].

Donor doping (such as Nb-doping) increases the domain wall mobility by reducing the polar defect complexes and hence by lowering the oxygen vacancies. As a result, the softening happens. On the other hand, acceptor doping such as Fe-doping creates a defect complex between Fe-substitutional defects and charged oxygen vacancies. This leads to a hardening effect [2]. From the results presented here (Fig. 5), an increase in the coercive field with doping concentration is observed. The values of $2 \times E_c$ are found to be 25.54, 28.80, 30.32, 32.85 and 35.39 kV/cm for NF0, NF2, NF4, NF6 and NF8 respectively. In dielectric response study, it is observed that the value of dielectric constant decreases and dielectric loss increases (at lower frequencies but decreases at higher frequencies) with doping concentration though the change in the loss with frequency is not as high as expected

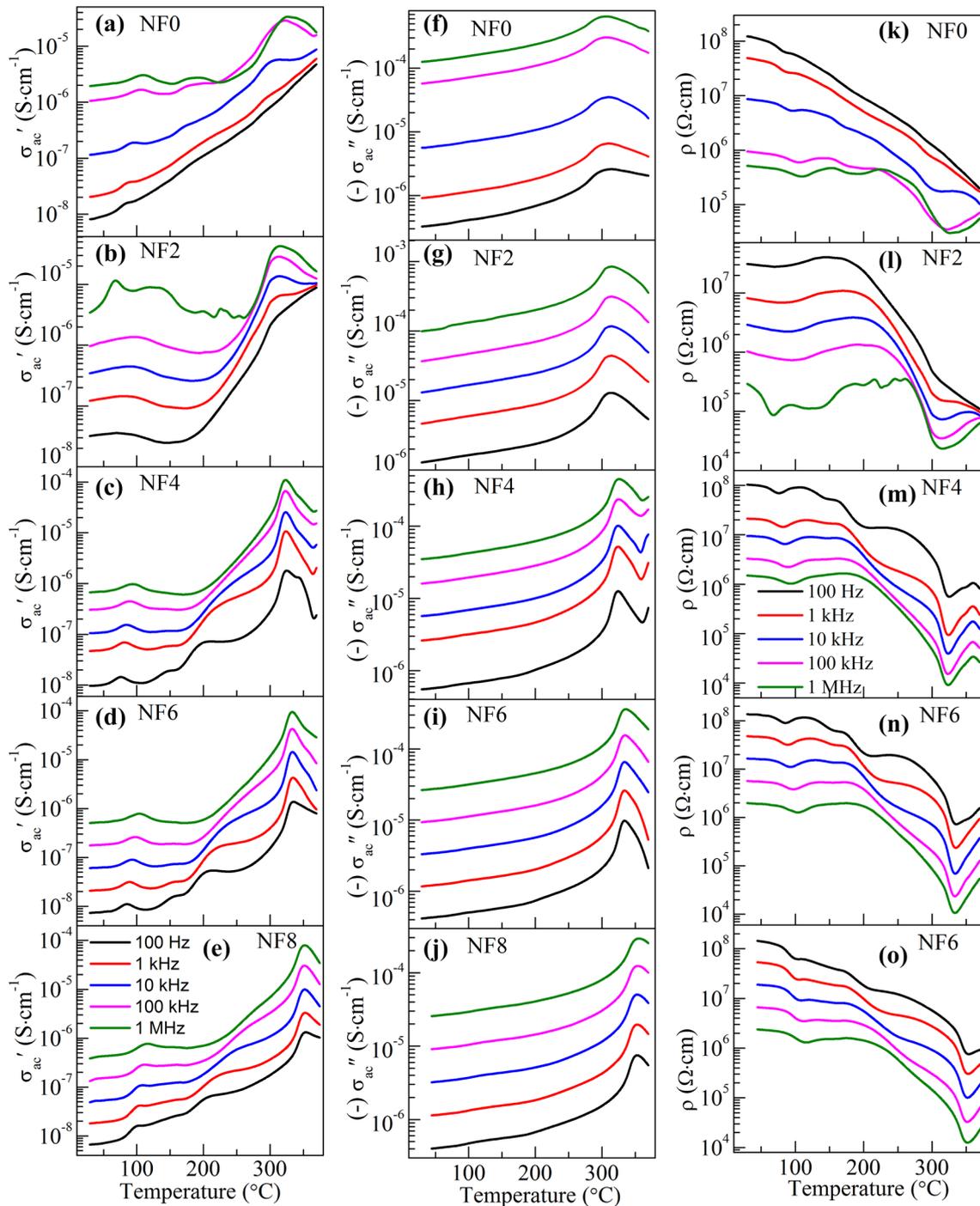


Fig. 4 AC conductivity and specific resistance of Nb and Fe codoped PLZT. Temperature dependence of ac conductivity (real part) (a–e), ac conductivity (imaginary part) (f–j) and specific resistance

(k–o) for different frequencies. (color legends/frequencies are the same for all parts of the figure)

for the softening effect. Hence, both these observations on polarization and dielectric response indicate the hardening effect [24–27].

In order to find out the “true switchable polarization”, also called as “non-volatile polarization” (as the

$2 \times P_r = P_r - (-P_r)$ is practically not the actual switchable polarization). Positive up negative down (PUND) test is carried out. In contrast with the general hysteresis measurement, for PUND test, the signal consists of five sharp pulses (one preset and four measurements) are used (Fig. 6a).

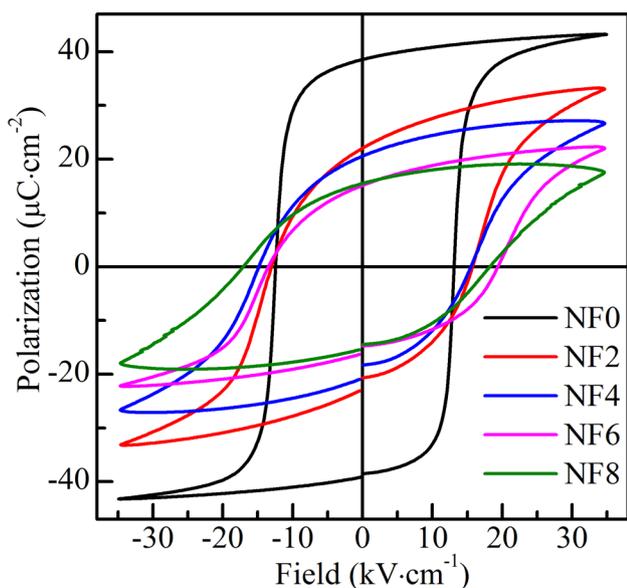


Fig. 5 Ferroelectric hysteresis (P-E) loops recorded at room temperature for Nb and Fe co-doped PLZT (NF0, NF2, NF4, NF6 and NF8)

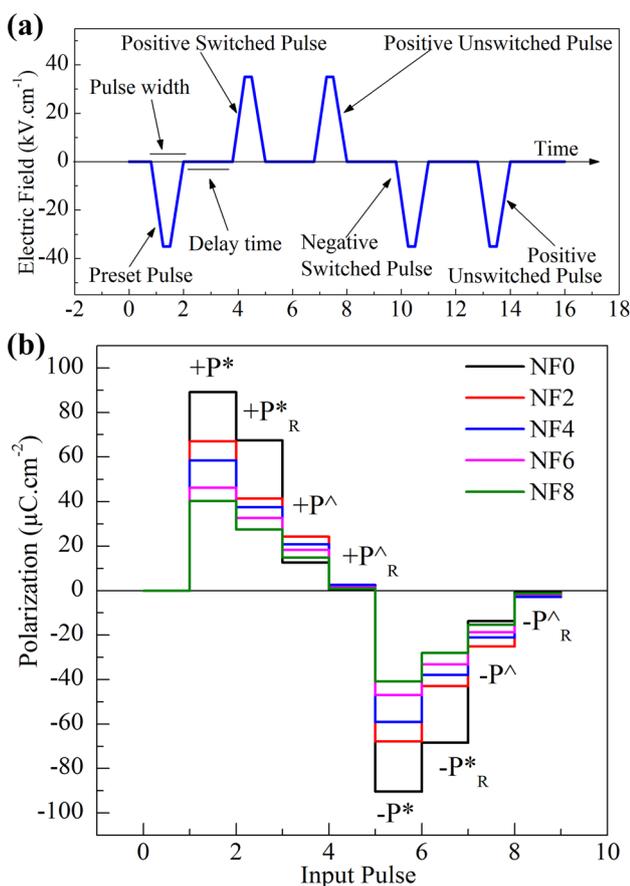


Fig. 6 **a** Input signal used for PUND measurement (representative only). **b** PUND test results for Nb and Fe co-doped PLZT (NF0, NF2, NF4, NF6 and NF8)

These pulses are: one negative preset pulse followed by two positive pulses (positive switched pulse and positive unswitched pulse). The positive unswitched pulse is followed by two negative pulses (negative switched pulse and negative unswitched pulse). The PUND test results for the pulses of the magnitude of 35 kV/cm are shown in Fig. 6b. The polarizations measured at those pulses are termed as switchable polarization (P^*), remnant switchable polarization (P^*_R), non-switchable polarization (P^\wedge) and remnant non-switchable polarization (P^\wedge_R), following the convention as described in the “Understanding Ferroelectric Materials” by Evans Jr [28].

The true switchable polarization (P_{sw}) is defined as, $P_{sw} = P^* - P^\wedge$. The calculated values of P_{sw} are plotted w.r.t. doping concentration and are shown in Fig. 7. It is found that the value of P_{sw} decreases with doping and the values are 76.57, 42.73, 37.49, 27.93 and 25.38 $\mu\text{C}/\text{cm}^2$ for NF0, NF2, NF4, NF6 and NF8 respectively. Generally, the $\pm P^\wedge_R$ (s) are expected to be equivalent to the loop-gap (gap between the start and end points of the hysteresis loop). The observed values of $\pm P^\wedge_R$ are 0.58(- 0.76), 2.12(- 2.74), 2.54(- 2.87), 1.42(- 1.68) and 0.97(- 1.32) $\mu\text{C}/\text{cm}^2$ while the values of loop-gap are 0.66, 2.38, 2.72, 1.50 and 1.06 $\mu\text{C}/\text{cm}^2$ for NF0, NF2, NF4, NF6 and NF8 respectively. Hence, this indicates a reasonable agreement with the expectation. In the case of a leakage-free material, $P_{sw} = (2 \times P_r - \text{loop-gap})$ can be expected. In our study, the values of P_{sw} are marginally less than the values of $(2 \times P_r - \text{loop-gap})$. The differences between these two quantities (i.e. $(2 \times P_r - \text{loop-gap}) - P_{sw}$) are 0.41, 0.97, 1.37, 2.02 and 4.41 $\mu\text{C}/\text{cm}^2$ for NF0, NF2, NF4, NF6 and

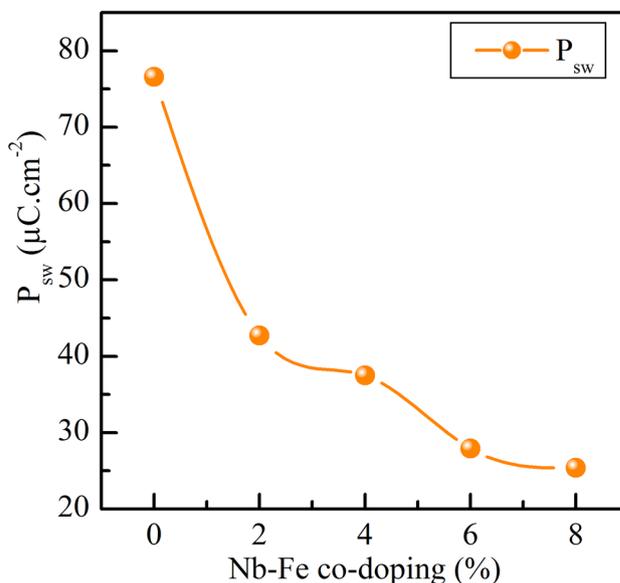


Fig. 7 Change in “true switchable polarization” (P_{sw}) with doping concentration for Nb and Fe co-doped PLZT (NF0, NF2, NF4, NF6 and NF8). (The solid line is to guide the eyes)

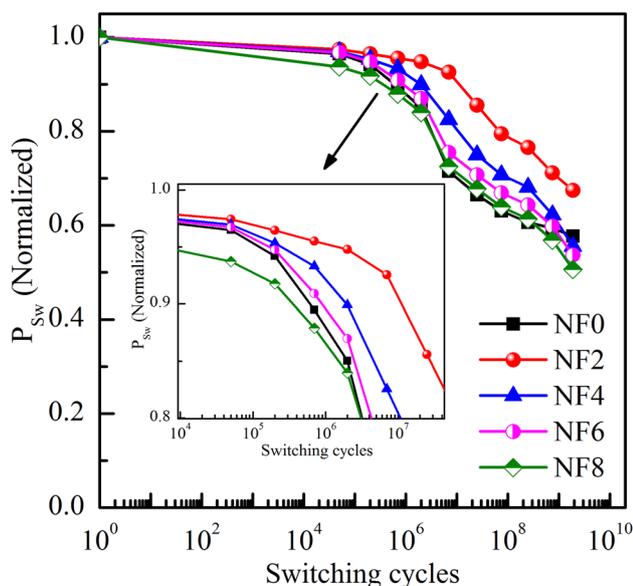


Fig. 8 Fatigue behavior (“true switchable polarization” (P_{sw}) vs switching cycles) for Nb and Fe co-doped PLZT (NF0, NF2, NF4, NF6 and NF8)

NF8 respectively. This signifies the effect of increasing leakage current. However, fatigue behavior is found to be improved with doping. Lowest fatigue is observed for NF2 (Fig. 8). The value of P_{sw} for NF2 is decreased by 5% at 7×10^5 cycles of switching whereas the decrement is 15% in case of NF0. The samples NF4 and NF6 show values between that of NF0 and NF2. NF8 performs lower than NF0. The enhancement in the resistance against fatigue observed for 2% Nb–Fe doping is somewhat similar to the behavior observed for single element doping. Haccart et al. reported enhanced fatigue behavior for 2% of Nb doping in PZT(54/46) [29]. Doping of WO_3 (used for ferroelectric softening) in PZT(52/48) thin film resists fatigue up to 10^8 cycles but similar doping of CuO (for hardening) doesn’t show such improvement, moreover shows fatigue at 10^5 cycles where undoped one shows at 10^6 cycles [30]. Hence, the enhanced fatigue resistance in NF2 could be due to the presence of 2% Nb; but as doping concentration increases the effect of Fe becomes dominant over the other.

The leakage current vs. electric field data is plotted in Fig. 9. The leakage current density is found to increase with co-doping of Nb and Fe in PLZT lattice. Leakage current sharply increases with the electric field up to the field close to the coercive field. On further rising of the field, it decreases marginally followed by an increase in higher fields. The rate of increment at the higher field is higher for higher doping. For NF8, sharp increase at field above 20 kV/cm is noticeably higher than that of other samples. This can be correlated to the observation of decreasing polarization at the higher field for NF8 (as explained before).

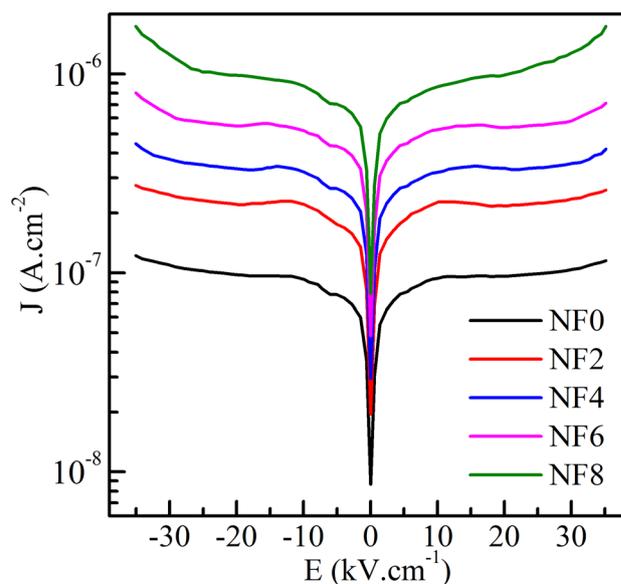


Fig. 9 Leakage current (J) versus electric field (E) at room temperature for Nb and Fe co-doped PLZT (NF0, NF2, NF4, NF6 and NF8)

3.5 Energy storage density

The energy storage density is calculated following the method reported by Zhao et al. [31]. The energy input during charging to the maximum polarization is defined as

$$\Delta J_{in} = \int_0^{P_{max}} EdP \quad (4)$$

where P is the polarization at an electric field E . The recoverable energy ΔJ after charging to the maximum polarization is defined as

$$\Delta J = - \int_{P_{max}}^{P_r} EdP \quad (5)$$

Hence, the efficiency η is defined as

$$\eta = \frac{\Delta J}{\Delta J_{in}} \quad (6)$$

The sample NF0 exhibits recoverable energy storage density of 58.84 mJ/cm^3 with an efficiency of 0.24. The comparable remnant and maximum polarization and the large hysteresis loss is the reason for this low value of ΔJ and η . But, in the case of NF2, as the P_r becomes lower than the P_{max} , the values of ΔJ and η become greater than that of NF0. The observed values of ΔJ and η for NF2 are 134 mJ/cm^3 and 0.28. The values are shown in Fig. 10. Upon increasing the doping concentration both

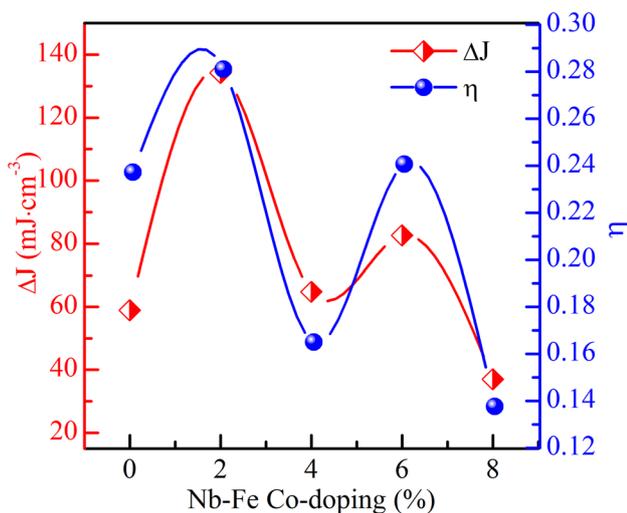


Fig. 10 Energy storage density (ΔJ) and efficiency (η) at room temperature for Nb and Fe co-doped PLZT (NF0, NF2, NF4, NF6 and NF8)

the polarization values decrease further and coercive field increases. As a result, both the ΔJ and η are found to decrease for NF4. Though for NF6, both the P_r and P_{max} decrease, due to the internal bias field the asymmetry arises in the coercive field, which causes an increase in ΔJ and η with respect to those of NF4. It was observed earlier that internal bias field at higher fields (above 20 kV/cm) affect the polarization of NF8; hence, polarization at higher fields become lower than the polarization observed around 20 kV/cm. This leads to a decrease in ΔJ and η . As a result of the complex effect of several factors, the values of ΔJ and η do not follow any regular trend of change with Nb–Fe co-doping in PLZT.

4 Conclusions

Temperature and frequency dependence of dielectric response, ac conductivity, specific resistance are studied for Nb and Fe co-doped PLZT ceramics. Ferroelectricity and dielectric properties are correlated with microstructure. The microstructures, both on surface and interior (well below the surface) are investigated. Microstructure inside the samples is different from the surface morphology and grains are much smaller inside the sample with respect to that on the surface. Polarization is found to decrease with doping, while the coercivity increases. The true switchable polarizations are calculated from the data obtained by PUND tests. The 2% Nb and Fe codoping show enhancement in fatigue resistance. Leakage current

is observed to increase with doping and the effect of internal bias field at the higher fields for higher doping is also seen. The recoverable energy storage density and efficiency do not follow any regular relation with doping concentration. The change in these quantities is directly depending on maximum polarization, remnant polarization, coercive field and hysteresis loss. The highest recoverable energy storage density is 134 mJ/cm³ with an efficiency of 0.28 for 2% Nb–Fe co-doped PLZT.

Compliance with ethical standards

Conflict of interest The authors declare that they have no conflict of interest.

References

1. K. Carl, K.H. Hardtl, *Ferroelectrics* **17**, 473–486 (1977). <https://doi.org/10.1080/00150197808236770>
2. A. Chandrasekaran, D. Damjanovic, N. Setter, N. Marzari, *Phys. Rev. B* **88**(214116), 1–7 (2013). <https://doi.org/10.1103/PhysRevB.88.214116>
3. D. Damjanovic, *Rep. Prog. Phys.* **61**, 1267–1324 (1998). <https://doi.org/10.1088/0034-4885/61/9/002>
4. R.D. Klissurska, K.G. Brooks, I.M. Reaney, C. Pawlaczyk, M. Kosec, N. Setter, *J. Am. Ceram. Soc.* **78**, 1513–1520 (1995). <https://doi.org/10.1111/j.1151-2916.1995.tb08846.x>
5. S.-Y. Chu, T.-Y. Chen, I.T. Tsai, *Integr. Ferroelectr.* **58**, 1293–1303 (2003). <https://doi.org/10.1080/10584580390259498>
6. W.I. Lee, J.k. Lee, *Mater. Res. Bull.* **30**, 1185–1191 (1995). [https://doi.org/10.1016/0025-5408\(95\)00137-9](https://doi.org/10.1016/0025-5408(95)00137-9)
7. A. Kumar, S. Reddy Emani, V.V. Bhanu Prasad, K.C. James Raju, A.R. James, *J. Eur. Ceram. Soc.* **36**, 2505–2511 (2016). <https://doi.org/10.1016/j.jeurceramsoc.2016.03.035>
8. B.W. Lee, E.J. Lee, *J. Electroceram.* **17**, 597–602 (2006). <https://doi.org/10.1007/s10832-006-8568-2>
9. S. Samanta, V. Sankaranarayanan, K. Sethupathi, M.S. Ramachandra Rao, *Vaccum* (2018). <https://doi.org/10.1016/j.vacuum.2018.08.053>
10. D. Mukherjee, M. Hordagoda, D. Pesquera, D. Ghosh, J.L. Jones, P. Mukherjee, S. Witanachchi, *Phys. Rev. B* **95**, 174304, (2017). <https://doi.org/10.1103/PhysRevB.95.174304>
11. H.-J. Kleebe, S. Lauterbach, L. Silvestroni, H. Kungl, M.J. Hoffmann, E. Erdem, R.d.-A. Eichel, *Appl. Phys. Lett.* **94**, 142901, (2009). <https://doi.org/10.1063/1.3103313>
12. S. Samanta, M. Muralidhar, V. Sankaranarayanan, K. Sethupathi, M.S. Ramachandra Rao, M. Murakami, *J. Mater. Sci.* **52**, 13012–13022 (2017). <https://doi.org/10.1007/s10853-017-1425-7>
13. D. Guo, K. Cai, Y. Wang, *J. Mater. Chem. C* **5**, 2531–2541 (2017). <https://doi.org/10.1039/c6tc04648g>
14. Z. Pan, L. Yao, J. Zhai, B. Shen, H. Wang, *Compos. Sci. Technol.* **147**, 30–38 (2017). <https://doi.org/10.1016/j.compscitech.2017.05.004>
15. V. Dimza, A.I. Popov, L. Lāce, M. Kundzins, K. Kundzins, M. Antonova, M. Livins, *Curr. Appl. Phys.* **17**, 169–173 (2017). <https://doi.org/10.1016/j.cap.2016.11.010>
16. A. Jonscher, *Dielectric Relaxation in Solids* (Chelsea Dielectrics Press Limited, London, 1983), p. 89
17. A.K. Jonscher, *J. Phys. D Appl. Phys.* **32**, R57–R70 (1999). <https://doi.org/10.1088/0022-3727/32/14/201>

18. D.P. Almond, C.R. Bowen, *Phys. Rev. Lett.* **92**, 157601, (2004). <https://doi.org/10.1103/PhysRevLett.92.157601>
19. J. Portelles, N.S. Almodovar, J. Fuentes, O. Raymond, J. Heiras, J.M. Siqueiros, *J. Appl. Phys.* **104**, 073511, (2008). <https://doi.org/10.1063/1.2988264>
20. S.K.S. Parashar, R.N.P. Choudhary, B.S. Murty, *Mater. Sci. Eng. B* **110**, 58–63 (2004). <https://doi.org/10.1016/j.mseb.2004.02.011>
21. B. Angadi, P. Victor, V.M. Jali, M.T. Lagare, R. Kumar, S.B. Krupanidhi, *Mater. Sci. Eng. B*, **100**, 93–101 (2003), [https://doi.org/10.1016/s0921-5107\(03\)00080-1](https://doi.org/10.1016/s0921-5107(03)00080-1)
22. M. Zheng, Y. Hou, Z. Ai, M. Zhu, *J. Appl. Phys.* **116**, 124110, (2014). <https://doi.org/10.1063/1.4896875>
23. W. Qiu, H.H. Hng, *Ceram. Int.* **30**, 2171–2176 (2004). <https://doi.org/10.1016/j.ceramint.2003.12.004>
24. L. Jin, Z. He, D. Damjanovic, *Appl. Phys. Lett.* **95**, 012905, (2009). <https://doi.org/10.1063/1.3173198>
25. R. Yimnirun, R. Wongmaneerung, S. Wongsanmai, A. Ngamjarrojana, S. Ananta, Y. Laosiritaworn, *Appl. Phys. Lett.* **90**, 112908, (2007). <https://doi.org/10.1063/1.2713769>
26. S. Zhang, J.B. Lim, H.J. Lee, T.R. Shrout, *IEEE Trans. Ultrason. Ferroelectr. Freq. Control.* **56**, 1523–1527 (2009). <https://doi.org/10.1109/TUFFC.2009.1215>
27. K. Prabakar, S.P. Mallikarjun Rao, *J. Alloys Compd.* **437**, 302–310 (2007). <https://doi.org/10.1016/j.jallcom.2006.07.108>
28. T. Joe. Evans Jr., *Hysteresis vs PUND - They are Equivalent (Understanding Ferroelectric Materials, Support documents, Radiant Technologies Inc.)* August 1, 2008, <https://www.ferrodevices.com/1/297/files/HysteresisEqualsPUND.pdf>
29. T. Haccart, D. Remiens, E. Cattan, *Thin Solid Films* **423**, 235–242 (2003). [https://doi.org/10.1016/s0040-6090\(02\)01045-3](https://doi.org/10.1016/s0040-6090(02)01045-3)
30. T. Sreesattabud, B.J. Gibbons, A. Watcharapasorn, S. Jiansirisomboon, *Ceram. Int.* **39**, S521–S524 (2013). <https://doi.org/10.1016/j.ceramint.2012.10.126>
31. X. Zhao, Z. Zhou, R. Liang, F. Liu, X. Dong, *Ceram. Int.* **43**, 9060–9066 (2017). <https://doi.org/10.1016/j.ceramint.2017.04.051>